

---

# Design and Simulation of a Back-to-Back Test Rig for Ultra High Cycle Fatigue Testing of Gears under Fully Reversed Load

**J. Lövenich, M. Trippe, O. Malinowski, J. Brimmers, S. Neus, C. Brecher**

Laboratory for Machine Tools and Production Engineering (WZL) of RWTH Aachen University

[The statements and opinions contained herein are those of the author and should not be construed as an official action or opinion of the American Gear Manufacturers Association.]

The paper was previously presented at the 2021 AGMA Fall Technical Meeting.



The authors gratefully acknowledge financial support by the Clean Sky 2 JU (Ref.-No. 831832) under Horizon 2020 program from the European Commission for the achievement of the project results.

## Abstract

Gear units for turbomachinery, especially in the aerospace sector, place high demands. In addition to the high power density, the demands are also increased regarding the operating temperatures compared to automotive applications. Furthermore, the high operating speed excites vibrations in the higher frequency range, which also poses challenges for the transmission design in terms of NVH. The high dynamics of over 12000 rpm combined with the high number of load cycles under fully reversed load ( $N > 10^8$ ) that an aviation planetary gearbox experiences makes load capacity tests with standardized back-to-back test rigs uneconomical or even impossible due to the extremely long testing times. To enable the Ultra High Cycle Fatigue (UHCF) testing, a high-speed back-to-back test rig was developed. In addition to the design, particular focus is placed on the thermal and dynamic simulation of the test rig. These two aspects are the basis for a safe commissioning and a successful testing. In the area of thermal simulation, the behavior of the test rig components in the operating temperature range from room temperature to  $T > 100^\circ\text{C}$  is investigated regarding the thermal expansion and the resulting tolerances. The dynamic simulation deals with the vibration behavior of the test rig. Special focus is placed on the tooth mesh frequency and the natural frequencies of the components. As a result, the operating points for testing are defined and the operational safety is ensured. In addition, for providing a basis for the investigation of aircraft transmissions, the paper shows fundamental ideas for the design of high-speed back-to-back gear test rigs.

Copyright ©2021

American Gear Manufacturers Association

1001 N. Fairfax Street, Suite 500

Alexandria, Virginia 22314

October 2021

ISBN: 978-1-64353-105-2

# Design and Simulation of a Back-to-Back Test Rig for Ultra High Cycle Fatigue Testing of Gears under Fully Reversed Load

J. Lövenich, M. Trippe, O. Malinowski, J. Brimmers, S. Neus, C. Brecher

Laboratory for Machine Tools and Production Engineering (WZL) of RWTH Aachen University

## 1 Introduction and Motivation

Geared turbofans provide a significant improvement in aero-engine efficiency by allowing the fan and turbine to rotate at their optimum speeds [1]. By lowering the fan pressure ratio, larger bypass ratios (BPR) of up to  $BPR = 12:1$  can be achieved [2]. For example, the PW1000G geared turbofan, displayed in Figure 1, which is installed in the short-haul aircraft Airbus A320neo, reduces fuel consumption and  $CO_2$  emissions by 16 % compared to the predecessor model. In addition, noise emissions can be reduced by 75 % due to the larger, slower fan [3]. With the turbine and fan rotating at different speeds, a gearbox is required to transfer a high level of torque within a restricted space to minimize the size of the engine core. Epicyclic gearboxes provide a space-efficient solution leading to a very high power transfer through the gears.

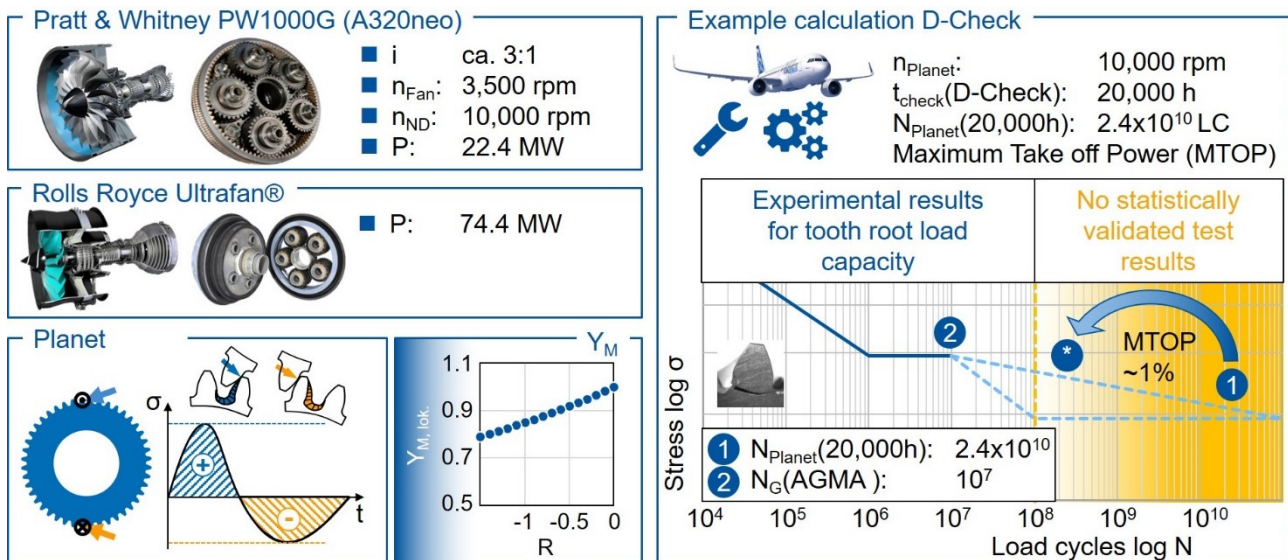


Figure 1 – Load cycles of geared turbofans and standards for tooth root load capacity [1; 2; 3; 4; 5; 6; 7]

Figure 1 illustrates the occurring number of load cycles of the gears of two different geared turbofans. Lufthansa currently performs engine overhauls on its A340s after about 20000 flight hours [6]. If this is calculated with the speed of a planet wheel in an exemplary planetary gear, the overall number of load cycles is  $N_{Plane} > 10^{10}$ . Assuming a percentage of 1 % with the maximum take-off power (MTOPTOP), the number of load cycles under full load is  $N_{MTOPTOP} > 10^8$ . As can be seen from the S-N curve shown in Figure 1, the number of load cycles  $N_{MTOPTOP}$  exceeds the limiting number of load cycles for tooth root bending strength according to ISO 6336 [4] and AGMA [5]. Pulsator test stands can achieve these high load cycles in shorter test times, but they do not offer the possibility of testing gears under fully reversed bending loads. Therefore, a high-speed back-to-back test rig must be developed to investigate the tooth root bending strength of aircraft gearboxes.

The high dynamics of the test rig require design adaptations compared to a back-to-back test rig according to DIN ISO 14635 [26]. In order to be able to classify the additional dynamic forces and the influence of the test speed on the load capacity, a functionally identical prototype with a lower performance class is built up. In a multi-body simulation, the prototype is dynamically mapped to compare the simulated additional dynamic loads with the dynamic factor  $K_V$  from ISO 6336.

---

In addition to the dynamic behavior of the test rig, the focus is particularly on thermal behavior. The strong temperature differences between the bearing injection temperature  $T = 40^{\circ}\text{C}$  in the test gearbox and the lubrication of the test gears at  $T = 140^{\circ}\text{C}$  result in a strong temperature gradient in the test gearbox housing. For this reason, the thermal expansions of the test rig, especially at the narrow sealing gaps, are considered in a thermal simulation with ANSYS.

## 2 State of the Art

### 2.1 Dynamic Tooth Forces in Gearboxes

The torsionally elastic gear system is excited to vibrations by the varying tooth mesh stiffness, modified tooth flanks and the course of the external load [4, 20, 22, 35]. During operation, this vibration excitation leads to dynamic tooth forces, which are superimposed, on the load from the static torque. During the transition from single to double tooth contact, there is a jump in the tooth force due to the changed mesh stiffness [12, 23]. At high loads, the influence of premature tooth engagement resulting from tooth deformation is also superimposed. The load magnification becomes maximum when the tooth meshing frequency coincides with the natural frequencies of the entire system [4, 7, 14, 19, 23, 27, 34, 35].

The additional dynamic loads due to the vibration excitation in the tooth mesh has been investigated in numerous works based on calculations and measurements. BOSCH developed a model to calculate dynamic tooth forces considering the periodically varying tooth mesh stiffness for variable speeds [4]. The calculation results were confirmed by measurements of the dynamic tooth forces using strain gauges. WINKLER carried out metrological investigations on the dynamic load overload of high-speed gears on a high-speed back-to-back test rig with up to  $n_{in} = 15,000$  rpm [35]. Based on the results of the investigations, WINKLER developed a calculation model for quantifying the dynamic additional loads of spur and helical gears. RETTIG carried out investigations on a back-to-back test rig up to  $n_{in} \approx 6000$  rpm on the pinion [35]. Based on the results of RETTIG's and WINKLER's investigations, RETTIG developed a simplified calculation method for determining the average additional dynamic loads in the sub- and supercritical speed range as well as the main resonance [34]. The corresponding calculation principles were later transferred into the standard calculation of DIN 3990 and are today the basis for the calculation of the  $K_v$  factor of ISO 6336 [24, 27].

GERBER investigated the internal additional dynamic loads and the gear damping. Partial eradication of vibration energy is due to damping in the drive train. Bearing friction, flow resistance and damping in the tooth contact play a role. Damping in the tooth contact is determined by the elasto-hydrodynamic conditions and is strongly dependent on the lubricant film properties. For conventional forged steels, the material damping compared to the lubricant-damping is negligible. In this case, mesh geometry, speed ratios and lubricant viscosity are the main influencing variables. [13]

The described additional dynamic loads can lead to premature failure of the gears and to noise excitation during operation. In method B of ISO 6336, the gear stage is transformed into a single-mass oscillator and the vibration behavior is assessed, see Figure 2. However, this model approach is often not sufficient, since the vibrations excite the entire drive train and thus in turn influence the vibration amplitude and frequency. The course of the actual torque fluctuation is approximated in the calculation according to ISO 6336 by a linear course of the  $K_v$  factor. Drive train-dependent resonance points in the sub- and supercritical range are not taken into account. [27]

In addition to the standard-based calculation methods, there are numerous works on the calculation of the additional dynamic loads. BAUD ET AL. used an electrical test rig to investigate the dynamic additional loads. The simulation program set up to calculate the additional dynamic loads was successfully validated. The comparison of the simulation and measurement results shows that a detailed model taking into account all degrees of freedom is necessary for the correct calculation of the dynamic tooth root stress. [3]

Furthermore, for the computational investigation of highly dynamic contact processes in gear drives, an FEM computational model exists that allows the consideration of impact processes, but requires higher computation times than a quasi-static tooth contact analysis [9]. The program system DZP (Dynamic Tooth Forces Program) allows the calculation of the dynamic load distribution of a single stage under consideration of multidimensional rotational and translational degrees of freedom [12, 16]. In this case, the tooth meshing stiffness is calculated according to analytical approaches. The calculation of the force excitation is carried out for the limiting case of an infinite rotational speed, whereby the differential equations for calculation can be simplified [12, 16].

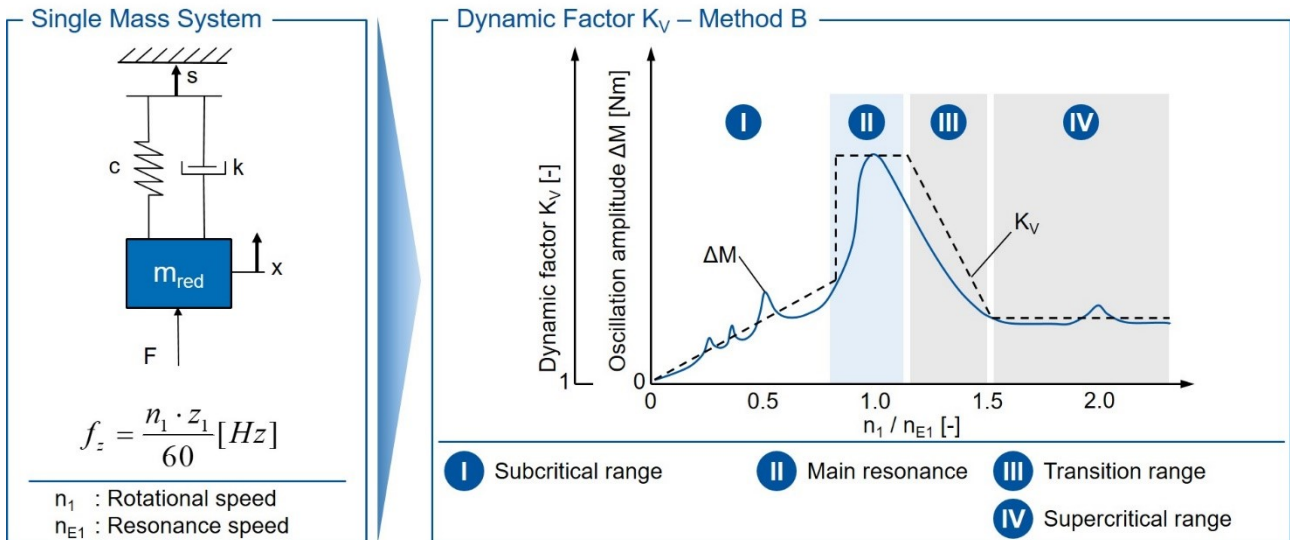


**Figure 2 – Influence of the rotational speed on the dynamic tooth root stress [ISO06b, BREC19]**

The force coupling element developed by GACKA and CARL allows the mapping of the dynamic excitation in the tooth meshing for a rotational vibration model using the FE-based mesh stiffness of the gear [5, 11]. Furthermore, modules integrated in the multibody simulation are available to represent the gear using analytical approaches [30, 33]. FRÜH combined the analytical contact calculation in six degrees of freedom with the FE-based mesh stiffness to model the gear meshing [10]. Thereby, displacements of the gears can be converted into changed contact distances and considered in the calculation of the stiffness [10].

In summary, it can be stated that with the help of the multi-body simulation, the dynamic additional loads in operation can be quantified in detail as a function of the speed. Depending on the selected discretization of the drive train, either the calculation of the maximum dynamic additional load or the course of the dynamic additional load over a gear meshing is possible. The determination of the course of the dynamic additional load for a tooth mesh enables the additional load to be converted into a dynamic tooth root stress. Furthermore, the correct quantification of the dynamic additional loads needs the consideration of all six degrees of freedom.

### 3 Design of the Ultra High Cycle Fatigue Back-to-Back Test Rig

In addition to the UHCF back-to-back test rig a functionally identical prototype with a lower performance class is built, in order to be able to classify the dynamic additional forces and the influence of the test speed on the load capacity [31]. In the following the mechanical structure of the prototype test rig as well as of the main test rig and the thermal conditions are described.

#### 3.1 Mechanical Structure of the Prototype

The design of the high-speed back-to-back test rig is comparable with the standardized test rigs from the ISO 14635 [26]. The test rig is divided into a test gearbox (2) and a reference gearbox (3), see Figure 3. The two gearboxes are connected to each other by shafts (7-10) and form a power circuit into which the test torque is applied. The maximum operating speed of the test rig is  $n_{in,max} = 12000$  rpm and the maximum operating torque  $M_{test,max} = 200$  Nm. The operating parameters allow the efficient investigation of the tooth root load capacity in the Ultra High Cycle Fatigue (UHCF) range.

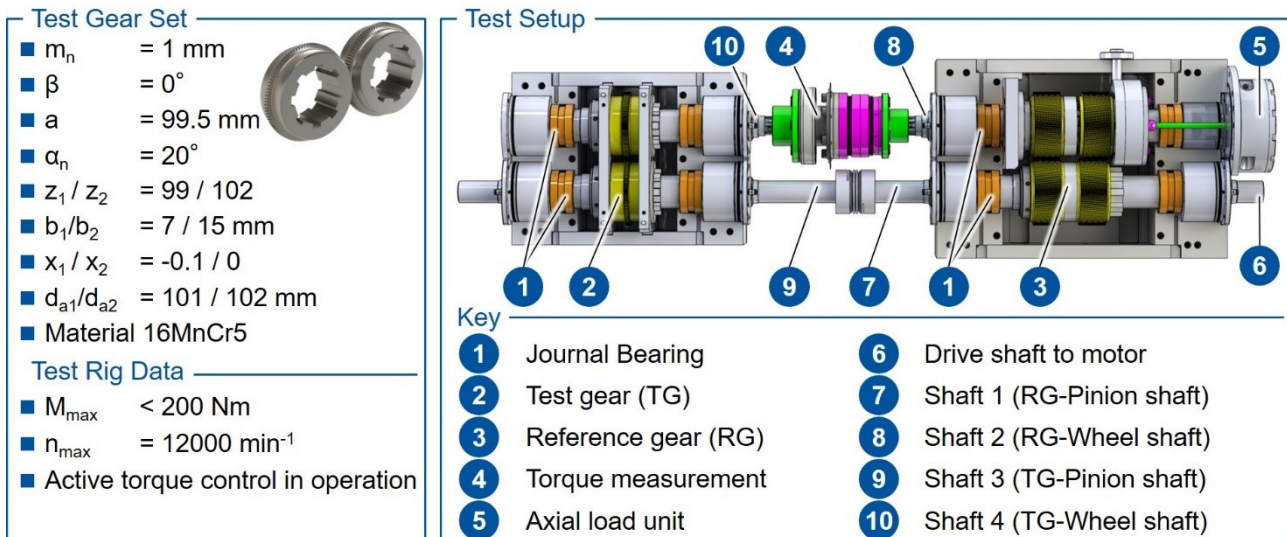


**Figure 3 – Design of the prototype test rig [31]**

Due to the expected load peaks in the event of tooth root fractures during operation and the high operating speed, the test rig was equipped with journal bearings (1). As a result, the test torque can only be applied from the limit speed of the journal bearings, at which pure fluid friction is present. The usual load application on standardized back-to-back test rigs by rotating the shafts by means of levers and weights at standstill is therefore not used [26, 31]. Instead, the test torque is applied and controlled by the axial displacement of a helical gear in the reference gear [31]. This system allows a compact design with high torsional stiffness and has been successfully used several times for driving high-speed back-to-back test rigs [6, 17]. Double helical gears are used to compensate for the axial forces in the reference gearbox. The forces to displace the helical gears are applied by an axial load unit (5). The displacement of the gear is made possible by a splined connection with clearance fit. For the non-shiftable gears, a splined connection with press fit is used. A torque measuring flange (4) in the power circuit measures the actual torque for control. In order to achieve complete compensation of thermal axial expansions of the shafts and to avoid constraining forces in the double helical gears, only the wheel shaft is axially supported in the reference gearbox (8) [31].

The test gear used is designed critically with regard to tooth root fracture. The gear data is shown in the left part of Figure 3. In order to operate the test rig with an unchanged infrastructure compared to conventional back-to-back test rigs, the maximum power in the power circuit was limited to  $P_{\max} = 250 \text{ kW}$  [31]. Due to the high drive speeds, the maximum test torque is  $M_{\text{test,max}} = 200 \text{ Nm}$ . It follows that the module and the tooth width of the test gears with  $m_n = 1 \text{ mm}$  and  $b = 7 \text{ mm}$  are small compared to the standardized gear geometries [26]. The gears in the reference gearbox are helical with  $\beta = 18^\circ$ . To keep the number of teeth and the center distance the same, the normal modulus was reduced to  $m_{n,VG} = 0.95 \text{ mm}$ .

### 3.2 Mechanical Structure of the Main Test Rig

The mechanical structure of the main test rig differs from the prototype. The main test rig has a three-shaft structure for implementing the reverse bending load, see Figure 4. There are no differences in the mode of operation, for example the load application by axial shifting of double helical gears or the use of journal bearings. The upscaling of the test rig allows a power increase to  $P > 5 \text{ MW}$  at the same operating speed of  $n = 12000 \text{ rpm}$  by increasing the maximum torque to  $M < 4000 \text{ Nm}$ .

### Test rig data

- $P > 5 \text{ MW}$
- $n \geq 12000 \text{ rpm}$
- $M > 4000 \text{ Nm}$
- $T_{\text{Oil, inlet}}: 90^\circ\text{C} - 140^\circ\text{C}$
- $Q_{\text{oil}} > 750 \text{ l/min}$
- Center distance:  
 $200 \text{ mm} \leq a \leq 250 \text{ mm}$
- Gear type: spur gears

### Test conditions

- Investigations up to  
 $N = 5 \cdot 10^8$
- Active torque regulation

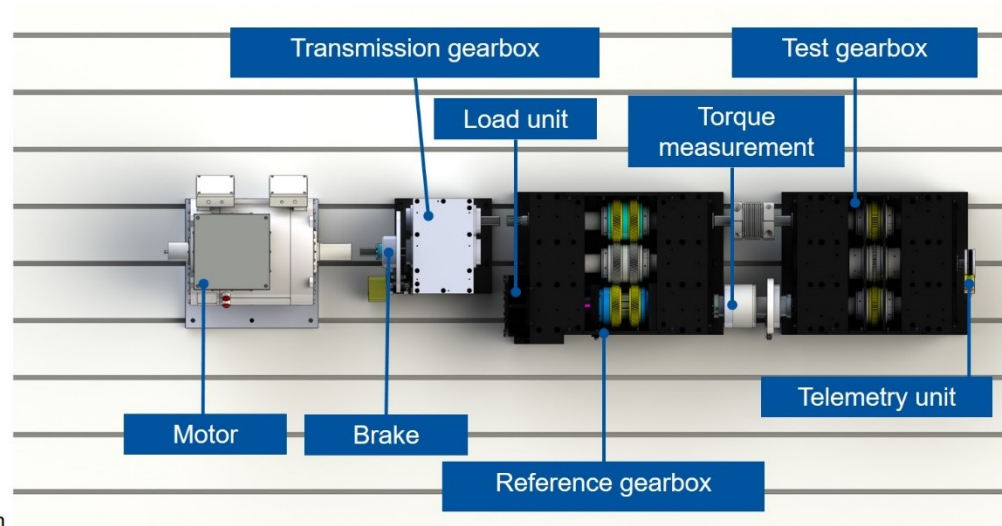
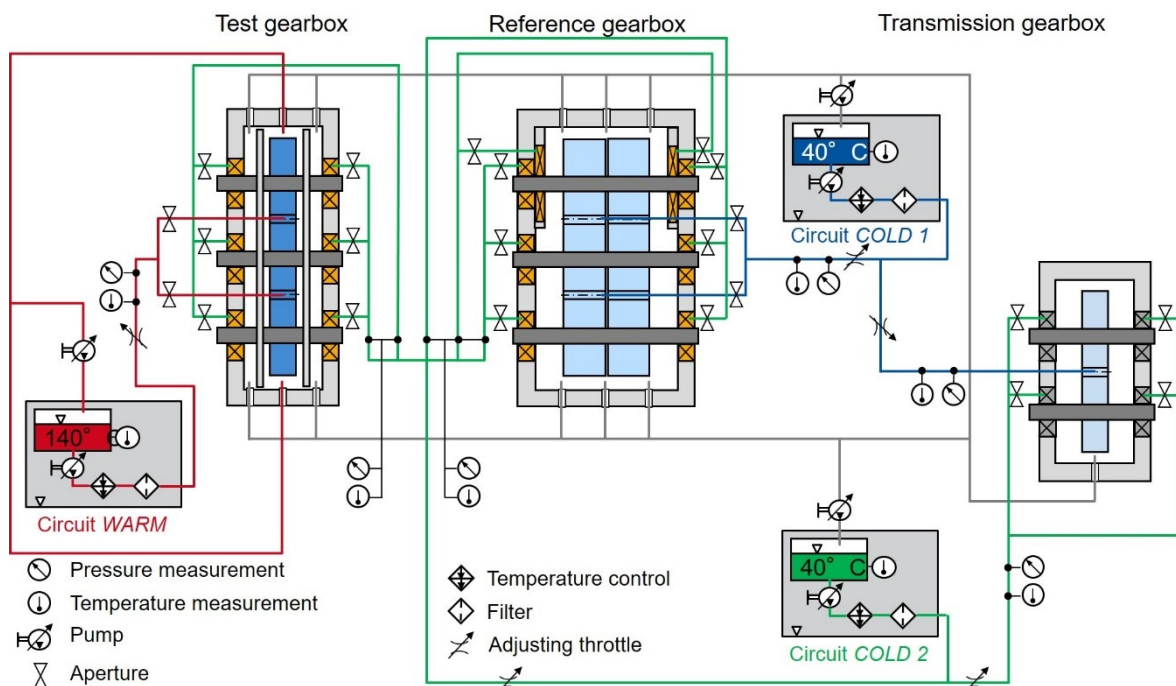


**Figure 4 – Design and power data of the main test rig for UHCF investigations under fully reversed bending**

### 3.3 Lubrication and Cooling System (Thermal Conditions)

The main test rig has a cooling and lubrication system to absorb a total power dissipation of  $P_{\text{loss, total}} = 390 \text{ kW}$ . For this purpose, a total volume flow of  $Q_{\text{oil, total}} = 733 \text{ l/min}$  is divided among 3 circuits, see Figure 5.



	Circuit WARM	Circuit COLD 1	Circuit COLD 2	$\Sigma$
$T_{\text{oil, in}}$	140°C	40°C	40°C	-
$T_{\text{oil, out}}$	160°C	61°C	60°C	-
$P_{\text{loss}}$	~80 kW	~225 kW	~85 kW	~390 kW
$Q_{\text{oil}}$	~190 l/min	~340 l/min	~200 l/min	~730 l/min

**Figure 5 – Cooling and lubrication system of the main test rig**

---

In accordance with the requirements from aviation gearboxes, the tooth mesh of the test gearbox is operated with an oil injection temperature of  $T_{\text{warm, in}} = 140^{\circ}\text{C}$  (warm circuit 1). The journal bearings of the test gearbox, the entire reference gearbox and the transmission gearbox are operated with an oil injection temperature of  $T_{\text{cold, in}} = 40^{\circ}\text{C}$  (cold circuit 1 & 2). The cold circuit is divided in 2 parts. Cold circuit 1 includes the cooling and lubrication of the reference and transmission gears. Cold circuit 2 includes the cooling and lubrication of the journal bearings of the test, reference and transmission gearbox.

## 4 Dynamic Simulation of the Test Rig

The dynamic simulation is carried out on the prototype, which has an identical design and mode of operation, but with a lower power class, see chapter 3, as this will be constructed and set up before completion of the main test rig in order to investigate the influence of the loading speed on the tooth root load capacity. The results are to be used to optimize the main test rig.

### 4.1 Structure and Basics of the Multi Body Simulation Model

The transfer of the prototype high-speed back-to-back test rig to the SIMPACK multibody simulation requires the simplification of the test setup. Figure 6 shows the test rig topology used. All shafts of the test rig are represented as elastic bodies with their natural frequencies in SIMPACK. The gears are represented as rigid bodies and the dynamic excitation and vibration behavior via SIMPACK GEAR PAIR.

The gears are coupled to the respective shafts with one degree of freedom in the direction of rotation. In the direction of rotation, a torsion-spring-damper element is used to represent the splined connection between the gear and the shaft. The shafts are mapped with six degrees of freedom. The journal bearings of the test rig are represented in a simplified way by cylindrical spring-damper elements with radial stiffness and damping. The damping of the journal bearings about the axis of rotation is considered via a torsion spring-damper without stiffness.

In deviation from the test rig setup, only one-half of the double helical gears is modeled in the reference gearbox. This is to avoid interference effects, for example due to uneven load distribution or axial vibrations. This means that both shafts in the reference gearbox must be axially fixed. For this purpose, the degree of freedom of the corresponding shafts is constrained in the axial direction. The permissibility of this assumption must be verified during commissioning. The axial fixing of the shafts in the test gearbox is carried out in the same way as in the test rig via the connecting clutches on the shafts and the reference gearbox shafts. The clutches connecting the shafts of the test and reference gearboxes are modeled as massless torsion-spring-dampers.

Since load application is also possible at standstill for the simulation, the application of the bracing torque is performed analogously to standardized back-to-back test rigs by rotating a test and reference gearbox shaft relative to each other. This procedure achieves a more stable calculation in comparison to the load application in reality by shifting helical gears. The iterative adjustment of the total torsion of the shafts leads to the desired torque on the test gears. The speed is controlled analogously to the test rig by applying a torque outside the power circuit. In the simulation, the drive torque is adjusted to produce a uniform speed increase over time. The vibration behavior is analyzed in the speed ramp-up from standstill to the operating speed of  $n_{\text{in}} = 12000$  rpm.

The parameterization of the coupling points used determines the calculated vibration behavior. For this reason, the stiffness and damping values are taken, as far as possible, from the data sheets of the components installed in the test rig or from the literature. However, there are uncertainties, particularly with regard to the damping values used and the stiffness of the spline shaft connections and journal bearings, which have to be assessed during commissioning.

**Table 1** shows the stiffness and damping values used to simulate the initial model. Where possible, the values were taken from the data sheets of the test rig components. These include the torsional stiffness of the couplings and the radial stiffness of the journal bearings.

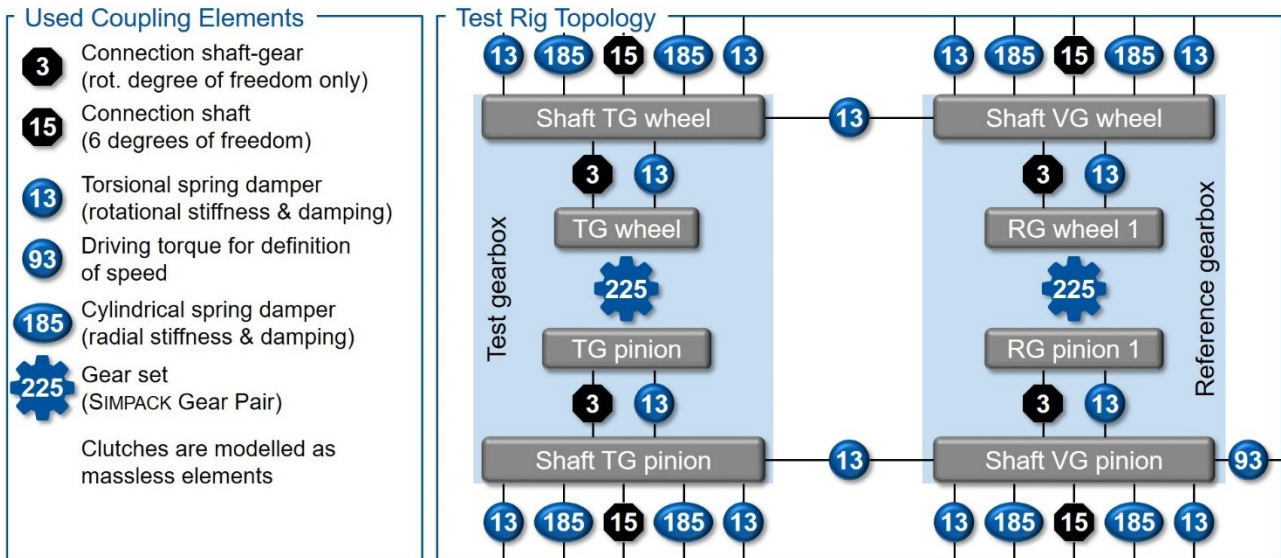


**Figure 6 – Topology of the prototype in the multi-body simulation**

**Table 1 – Reference values for stiffness and damping of the bearing and coupling points**

	Stiffness/Damping type	Value
<b>Journal bearings</b>	Stiffness radial	$10^8$ N/m
	Damping radial	$4 \cdot 10^4$ Ns/m
	Torsional damping	0.0007 Nms/rad
<b>Spline-hub connection</b>	Torsional stiffness	$10^6$ Nm/rad
	Torsional damping	$10^3$ Nms/rad
<b>Coupling (wheel)</b>	Torsional stiffness	$290 \cdot 10^3$ Nm/rad
	Torsional damping	600 Nms/rad
<b>Coupling (pinion)</b>	Torsional stiffness	$138 \cdot 10^3$ Nm/rad
	Torsional damping	300 Nms/rad
<b>Gears</b>	Gear meshing stiffness	acc. to DIN 3990
	Gear meshing damping	$10^3$ Ns/m

The torsional damping of the journal bearings was calculated approximately from the moment of loss at the operating point. The torsional damping of the couplings cannot be determined without measurements of the natural frequencies and vibration behavior. As an approximation, values below the damping of the splined shaft are therefore assumed, since there are fewer separation joints. Since the number of parting lines in the coupling package is doubled on the wheel side by integrating the torque measurement flange, the assumed torsional damping is also doubled. The meshing stiffness of the gears is calculated within the SIMPACK GEAR PAIR using the procedure of DIN 3990 [24]. The gear damping was determined according to the procedure of GERBER [13]. The torsional stiffness and damping of the spline connection was estimated using the values of WALTEN ET AL. and BARROT ET AL. [2, 32]. Since the system behavior is to be considered outside the resonance points in the supercritical range, only a small influence of the damping values is to be expected.

#### 4.2 System Behavior in Relation to the Operating Speed

The amount of dynamic torque fluctuation depends on the speed of the test rig. Since different gear geometries are used in the test and reference gearboxes due to the load application concept, the dynamic torque also



differs in the test and reference gearbox. The gears in the test gearbox have straight teeth and, due to the head shortening of the wheel, a total or profile contact ratio of  $\varepsilon_\alpha = \varepsilon_\gamma = 1.26$ . This results in a significant vibration excitation, which leads to high torque amplitudes in operation. Due to the helix angle of  $\beta = 18^\circ$  and the lack of head shortening, the gears in the reference gearbox have a total contact ratio of  $\varepsilon_\gamma = 5.59$ . It follows that the dynamic torque amplitudes in the reference gear are comparably small. To calculate the dynamic torque, in the first step the system is statically clamped to a torque of  $M_{R, \text{pinion}} = 180 \text{ Nm}$  at the pinion by rotating the shafts relative to each other. In the second step, a drive torque of  $M_{\text{an}} = 9 \text{ Nm}$  is applied. An S-function is used for continuous imprinting, which prevents discontinuities in the simulation. The drive torque leads to a continuous speed increase of the test rig. The sampling rate in the simulation is  $f_{\text{sample}} = 40 \text{ kHz}$ , so that the tooth meshing can be reproduced with sufficient accuracy even at high speeds.

The left part of Figure 7 shows the gear data and the modifications. To reduce premature tooth meshing and to optimize load distribution on the tooth flank, profile and width crowning were applied. The dynamic torque curves in the test and reference gear for a speed ramp-up of  $n_{\text{in}} = 0 - 12000 \text{ rpm}$  are shown in the right part of Figure 7.

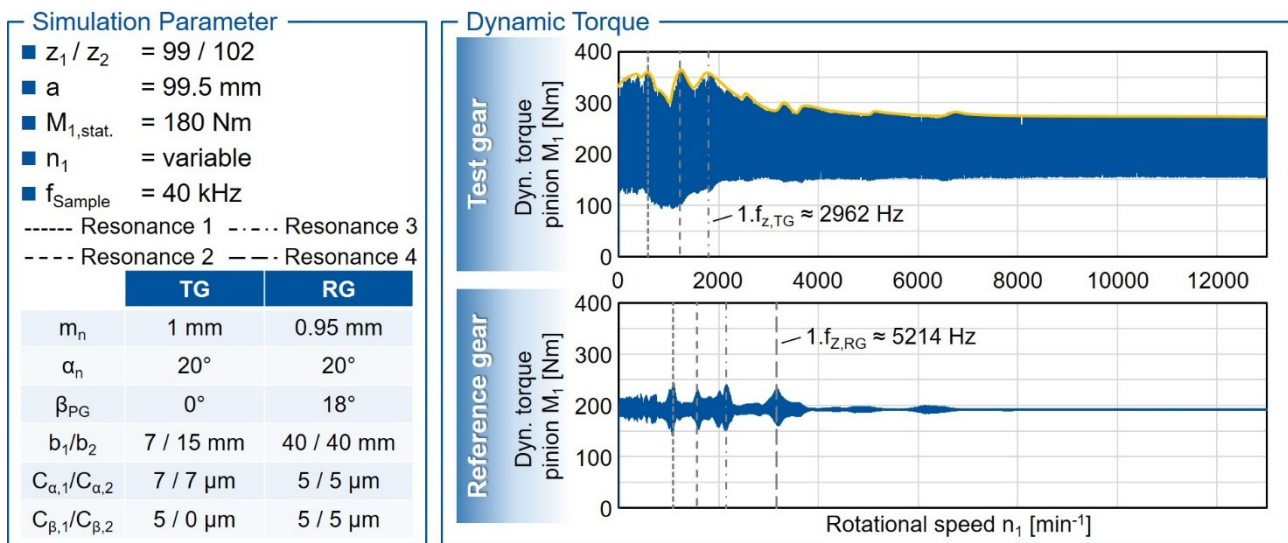


**Figure 7 – Analysis of the operational behavior over the rotational speed**

The maximum amplitude of the dynamic torque in the test gear unit with  $\Delta M_{\text{PG}} \approx 150 \text{ Nm}$  is significantly higher than the maximum amplitude of  $\Delta M_{\text{VG}} < 50 \text{ Nm}$  in the reference gearbox. The asymmetry of the torque curve in the test gear is due to the fact that a deflection to the maximum dynamic torque occurs only once in a tooth grip. Low dynamic torques account for the greater part of the values. In the dynamic torque curves of the test and reference gearbox, resonance points of the system are characterized by local torque maxima. The first three (TG) or four (RG) significant resonances are marked in the diagrams. The system is primarily excited from the rotational gear excitation in the test and reference gearbox. Accordingly, a large influence of the torsional natural frequencies on the system behavior is to be expected.

**Table 2** shows the first three torsional natural frequencies of the shafts in the test and reference gearbox. If the speed-dependent tooth mesh frequency  $f_z$  or multiples thereof coincide with the system natural frequencies, a local torque maximum occurs. The torque fluctuation up to the first resonance point in the test gear is due to the excitation of the bending natural frequencies of the pinion and wheel shafts by the 3rd and 4th  $f_z$ . At the second resonance point in the test gear, the first torsional natural frequency of the pinion shaft  $\omega_{T,1, \text{TG Pinion}}$  and the 2nd  $f_z$  coincide. The third resonance is caused by the excitation of the first torsional natural frequency of the wheel shaft  $\omega_{T,1, \text{TG Wheel}}$  with the 2nd  $f_z$ . After the third resonance, the maximum dynamic torque fluctuation decreases to an increased level of  $\Delta M_{\text{PG}} \approx 50 \text{ Nm}$  from  $n_{\text{in}} = 3000 \text{ rpm}$  and does not exhibit any further significant maxima.

Due to the overall smaller fluctuation of the dynamic torque, the resonances in the reference gearbox are more noticeable than in the test gearbox. The first resonance is caused by the encounter of the first torsional natural frequency of the pinion shaft  $\omega_{T,1, \text{RG Pinion}}$  with the 2nd  $f_z$ . At the second resonance, the 2nd and 3rd  $f_z$  excite the second torsional natural frequencies of pinion and wheel shaft  $\omega_{T,2, \text{RG pinion}}$  and  $\omega_{T,2, \text{RG wheel}}$ . At the third resonance, the first torsional natural frequency of the pinion shaft  $\omega_{T,1, \text{RG pinion}}$  meets the 1st  $f_z$ . Additionally, the

third torsional natural frequency of the pinion shaft  $\omega_{T,3,RG}$  Ritzel meets the 2nd  $f_z$ . The fourth and last significant resonance in the reference gear is due to the excitation of the second torsional natural frequency of the pinion shaft  $\omega_{T,2,RG}$  Pinion by the 1st  $f_z$ . From  $n_{in} = 4000$  rpm, the maximum dynamic torque amplitudes drop to a low level without further significant maxima. The comparison of the dynamic torque curves in the test and reference gearbox shows that, due to the long gear shafts, the gearboxes are not influenced by the dynamic loads or resonances in the other gearbox. Therefore, it would be permissible to focus solely on one gearbox for further analysis.

**Table 2 – Reference values for stiffness and damping of the bearing and coupling points**

	Shaft TG pinion	Shaft TG wheel	Shaft RG pinion	Shaft RG wheel
1s torsional natural frequency $\omega_{T,1}$	4022.7 Hz	5926.7 Hz	4887.5 Hz	3563.9 Hz
2nd torsional natural frequency $\omega_{T,2}$	5657.2 Hz	9482 Hz	7763.9 Hz	5092 Hz
3rd torsional natural frequency $\omega_{T,3}$	7776.4 Hz	12831 Hz	9646.9 Hz	6895 Hz

### 4.3 Definition of Operating Points of the Test Rig

In the first step, the additional dynamic load calculated in SIMPACK in the test and reference gearboxes is compared with the  $K_v$  factor according to ISO 6336 [27]. In the second step, the operating points of the test rig and possible strategies for the run-up to the operating speed are discussed.

#### 4.3.1 Comparison of Multi-Body-Simulation and Standardized Calculation Approach

In the load capacity calculation of gears, the dynamic additional load in operation are usually taken into account by means of the dynamic factor  $K_v$  of ISO 6336 presented in the state of the art [27]. Figure 8 compares the dynamic factors according to method B of ISO 6336 and the simulation in SIMPACK. For the comparison of the additional dynamic loads with the  $K_v$  factor calculation from the ISO 6336, the envelopes of the maximum dynamic torque are related to the mean torque to generate a speed dependent  $K_v$  factor from the SIMPACK simulation, see **formula 1**.

$$K_V(n_{An}) = \frac{M_{dyn,max}(n_{An})}{M_{dyn,MW}} \quad (1)$$

The upper diagram shows the additional dynamic loads in the test gear. According to ISO 6336, the resonance speed of the test gear is  $n_{E,TG} = 2,953.48$  rpm. In the subcritical range before the main resonance, the  $K_v$  factor according to ISO 6336 increases linearly up to a value of  $K_{v,ISO} = 1.25$  at  $n_1 = 2500$  rpm. The dynamic factor according to SIMPACK is in the same range above  $K_{v,Simpack} = 1.5$ . In the transition range to the main resonance as well as in the main resonance, the dynamic factor from ISO 6336 increases to values of  $K_{v,ISO} = 1.8 - 1.9$ . In contrast, SIMPACK calculates a lower dynamic factor of  $K_{v,Simpack} \approx 1.3$ . In the supercritical speed range from  $n_1 = 4,500$  rpm, the dynamic factor from ISO 6336 drops to a value of  $K_{v,ISO} = 0.87$  while the dynamic factor from SIMPACK remains at a level of  $K_{v,Simpack} \approx 1.2$ . The dynamic additional load in the subcritical and supercritical operating region is underestimated by the simplified standard calculation according to method B whereas the additional load in the main resonance is overestimated. This is because the additional loads in the test gear are determined by the excitation of the shaft natural frequencies in the subcritical speed range and not by the gear natural frequency. Furthermore, it is to be noted that the test gears represents a limiting case for the standard calculation due to the low total contact ratio of  $\varepsilon_{v,PG} = 1.26$ . In the supercritical region, there is a reduction of the maximum load in the single engagement area critical for the standard calculation. Due to the low profile overlap, however, higher additional loads are to be expected in real operation. In the calculation of the dynamic factor in SIMPACK, only the maximum occurring torque is taken into account and not the time of occurrence related to the tooth mesh.

The diagram below shows the comparison of the dynamic factors from the standard calculation and SIMPACK for the reference gear unit. Since the reference gear is a helical gear with  $\beta = 18^\circ$ , the total contact ratio of the reference gear with  $\varepsilon_{v,VG} = 5.59$  is considerably larger. The large total contact ratio results in a low vibration

excitation by the gears and correspondingly lower additional dynamic loads than in the test gear. The resonance speed of the reference gears according to ISO 6336 is  $n_{E,VG} = 3,069.1$  rpm and agrees with the value from SIMPACK. In the subcritical speed range, the dynamic factors from ISO 6336 and SIMPACK are approximately the same. In the main resonance, the dynamic additional load is also reproduced sufficiently accurately by ISO 6336 compared with the values from SIMPACK. In the supercritical speed range, ISO 6336 overestimates the dynamic additional load with a constant value of  $K_{V,ISO} = 1.32$  compared to SIMPACK ( $K_{V,Simpack} \approx 1.008$ ). This is because the  $K_V$  factor in the standard calculation cannot fall below one for a total overlap of  $\varepsilon_V = 2.5$ .

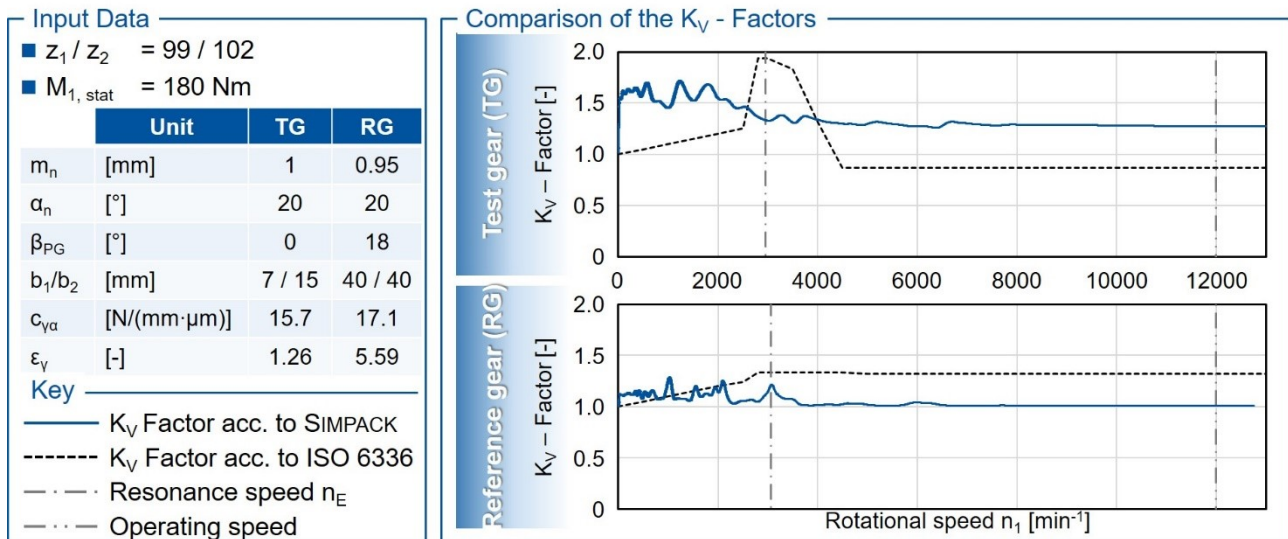


**Figure 8 – Comparison of the dynamic factors from SIMPACK and ISO 6336 [27]**

The comparison of the dynamic factors from ISO 6336 and SIMPACK shows that the standard calculation according to method B is not suitable for correctly representing the additional dynamic load in the operating range up to  $n_1 = 12000$  rpm. This can be explained on the one hand by the special geometry of the test gears and on the other hand by the influence of the shaft natural frequencies. For this reason, the dynamic factor calculated with SIMPACK is used to define the operating points of the test rig. For the final evaluation of the results from SIMPACK, it is necessary to convert the additional dynamic loads into the dynamic tooth root stress.

### 4.3.2 Definition of the Operating Points for the Investigation of the Tooth Root Load Capacity

The desired operating speed of the test rig is  $n_{test} = 12000$  rpm. The analysis of the vibration behavior has shown that no resonances occur above a speed of  $n_1 = 4000$  rpm. Accordingly, operation at the desired operating speed is feasible. The additional dynamic load at this speed must be taken into account when calculating the tooth root stress. To compare the tooth root stresses of different test rigs, it is necessary to calculate the additional dynamic loads using a simulation model and to transfer the additional dynamic loads to the dynamic tooth root stress. The simulation results also show that the definition of discrete torque levels is necessary for the speed ramp-up of the test rig up to the operating point, since otherwise pre-damage of the gears is likely due to the high additional loads in the subcritical speed range, see Figure 9.

At standstill, the minimum torque  $M_{min} = 10$  Nm is applied. This minimum tension serves to take out the backlash of the tooth flanks during speed ramp-up to the minimum bearing speed. In the second step, the speed is increased in a controlled manner to the transition speed of the journal bearings and kept constant at a speed level of  $n = 750$  rpm. In the 3rd step, the torque is increased to half the test torque  $M = 0.5 M_{test}$ . In step 4 the speed is increased to the maximum operating speed of  $n = 12000$  rpm.

During the speed ramp-up from  $n_{bearing,min} = 750$  rpm to  $n_{test} = 12000$  rpm, the main test rig resonances are run through, compare Figure 7 and Figure 8. Since the torque for ramp-up is significantly smaller than the test torque, no influence of the dynamic loads on the load capacity is to be expected. On the other hand the increased torque compared to the first step ensures permanent contact between the tooth flanks. The last step is increasing the torque to the test torque.

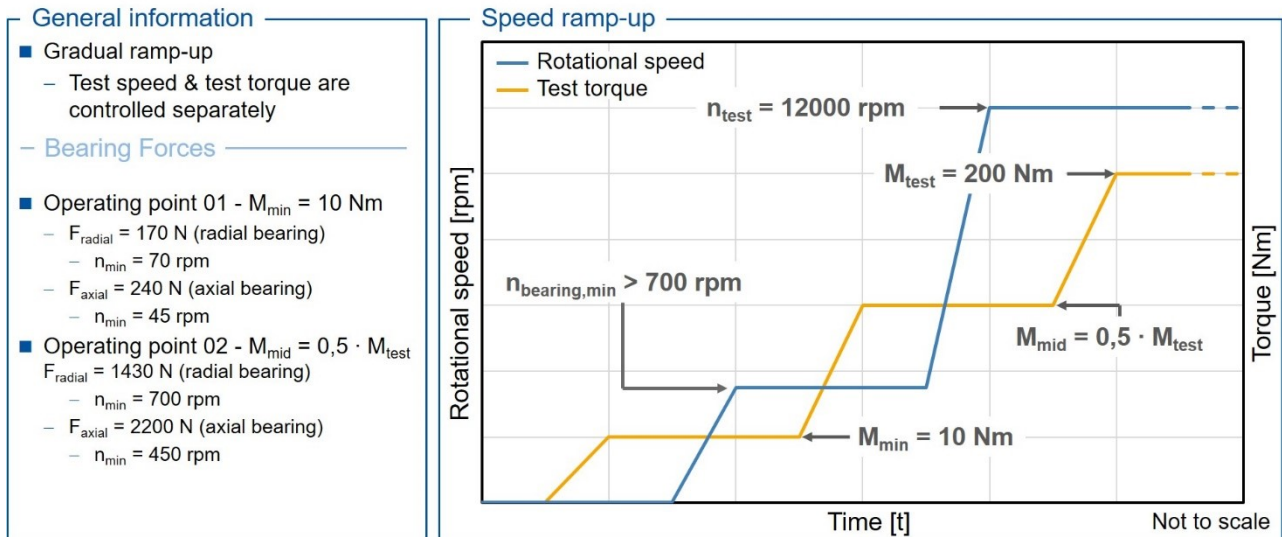


**Figure 9 – Speed and torque ramp-up for the prototype test rig**

#### 4.4 Conclusion of the Dynamic Simulation

The main purpose of the prototype test rig is to investigate the influence of the speed on the tooth root load capacity. The results of the dynamic simulation in SIMPACK show clear differences to the estimation of the dynamic loads according to ISO 6336. After the test rig has been set up, the main resonances are investigated experimentally by means of impact tests. Additionally during commissioning the main resonances are investigated, by vibration measurements directly on the rotating pinion shaft, and the dynamic mapping of the back-to-back test rig is validated in the multibody simulation. By validating the additional dynamic loads calculated in SIMPACK on the prototype, a separate multibody simulation model will be created for the main test rig so that, if necessary, design measures can be taken to change the natural frequencies of individual components before the main test rig is set up.

### 5 Thermal Simulation of the Test Rig

In addition to the dynamic behavior of the test rig, the focus is particularly on the thermal behavior. The temperature difference between the bearing injection temperature ( $T = 40^{\circ}\text{C}$ ) in the test gearbox and the gear injection temperature ( $T = 140^{\circ}\text{C}$ ) lead to a significant temperature gradient in the test gearbox housing. With regard to thermal expansion, the guarantee of function in the heated state must be ensured. In particular, the radial gaps at the seals must be considered. Another important point is the axial play of the mounted shafts, which is strongly dependent on the axial thermal expansion. For this purpose, the thermal behavior of the two gearboxes is simulated individually in ANSYS. In this report, however, the focus is on the test gearbox, as this is where the highest temperature differences occur.

#### 5.1 Structure and Basics of the Thermal Simulation Model

To simplify the model in ANSYS, all chamfers, screws and small radii are removed to prevent refinement of the mesh and thus greater computational effort on these. Furthermore, the spline profiles of the gear shafts and gears are removed. Holes and small gaps, for example gaps to avoid double fits, are plugged to optimize the meshing. In addition, individual bodies are grouped together to optimize meshing and reduce contact conditions, which in turn reduces computation time. The admissibility of the assumptions made must be verified by means of measurements in subsequent operation, as these do not necessarily take place on the safe side. The meshed model of the test gearbox and the meshing parameters are shown in Figure 10. Mainly square hexahedron elements are used. The test gearbox exists of overall 76,872 elements with 352,153 nodes. As input data, the gear losses according to NIEMANN/WINTER are assumed to be  $P = 500 \text{ W}$  for the pinion and

P = 250 W each for the wheels, which means that both tooth meshes have an individual loss of P = 500 W, which is split 50/50 between wheel and pinion [23].

**Mesh data**

- Mainly square hexahedron elements used

Elements:            76,872  
 Nodes:                352,153

**Input data**

- Boundary conditions in the "hot part" (T=160 ° C in the lower part of the housing, convection of the lubricating oil in the remaining part)
- Heat flow on gears: pinion: 500 W; wheels 250 W each (assumption that the pinion has two tooth contacts and the wheels each one)

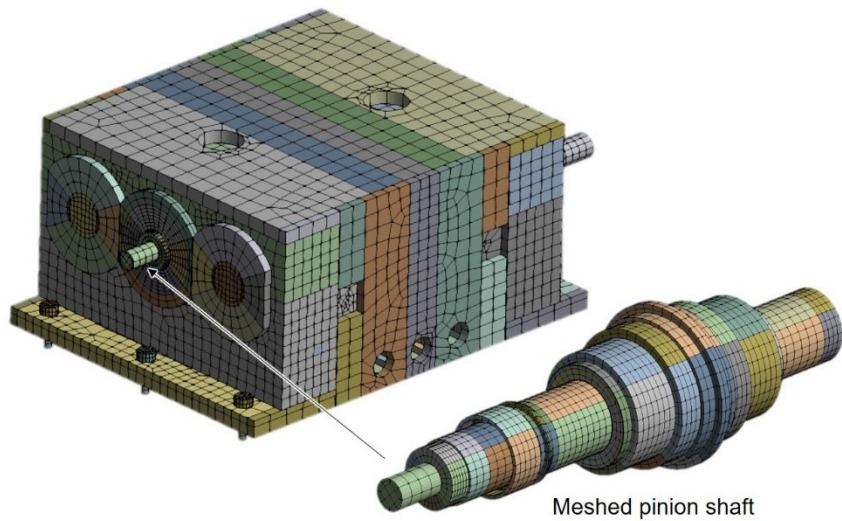


**Figure 10 – Meshed ANSYS model of the test gearbox**

### 5.1.1 Boundary conditions

The heat sources are the journal bearings and tooth meshes due to friction, compare power losses listed in chapter 3.3. Heat dissipation takes place on the one hand via the dissipation of the oil volume flow and on the other hand via convection and radiation of the housing and clamping field. In addition, the heat transfer within the housing must be considered.

#### Convection of the gearbox housing to the surrounding air

The convection from the housing to the environment is approximated according to NIEMANN/WINTER, compare **Formula 2** [23]. For this purpose, the surrounding air is assumed to be at rest.

$$\alpha_a = f_k \cdot (10 + 0.07 \cdot (T_G - T_u)) \cdot \left(\frac{1}{h}\right)^{0,15} \quad W/(m^2K) \quad (2)$$

$\alpha_a$	Heat transfer coefficient	W/m <sup>2</sup> K	$T_u$	Temperature of surrounding medium	K
$f_k$			$T_G$	Temperature of the component	K
$h$					

The test gearbox housing is divided into a cold area (blue) with an estimated temperature delta of  $\Delta T \sim 40$  K and a warm area (red) with  $\Delta T \sim 100$  K, compare Figure 11. The estimation was made on the basis of the injection temperatures. The ambient temperature is assumed to be T = 20°C. Accordingly, the heat transfer coefficients for convection from housing to air result in  $\alpha_{TG, warm} = 19.5$  W/m<sup>2</sup>K for the warm part and  $\alpha_{TG, cold} = 15.09$  W/m<sup>2</sup>K for the cold part of the housing.

#### Convection of the clamping field to the surrounding air

The clamping field can be displayed as plane surface and therefore the relationship for natural convection of the plane surface according to RECKNAGEL can be used [29]. With a temperature difference of  $\Delta T = 100^\circ K$  and a dimension of A = 1.6x4m (undisturbed area in front of the test gearbox housing), the heat transfer coefficient for convection of the clamping field to surrounding air is  $\alpha_{CF, TG} = 6.3$  W/m<sup>2</sup>K.

## Heat radiation from housing and clamping field to the surrounding air

According to GROßMANN/JUNGNICKEL, the emission coefficients  $\varepsilon_{\text{housing}} = 0.6$  (for a mat steel) and  $\varepsilon_{\text{clamping field}} = 0.94$  (For an unalloyed rough steel) can be assumed for the heat emission of the housing and clamping field via radiation to the surrounding air [18].

## Heat transfers within the test gear unit (oil convection and radiation) from the components to the housing

In the warm area, the emission coefficient for a thick layer of oil on polished steel is given as  $\varepsilon_{\text{oil, thick}} = 0.82$ . Radiation at the bottom is neglected (assumption: lake of oil so chaotic that radiation is difficult to determine and also negligible). The housing there has the temperature of the oil ( $T = 160\text{ °C}$ ), according to NIEMANN/WINTER with an oil injection temperature of  $T_{\text{oil, in}} = 140\text{ °C}$  and an  $\Delta T = 20\text{ °C}$  [23]. Also according to NIEMANN/WINTER, a heat transfer coefficient of  $\alpha_{\text{oil, TG}} = 300\text{ W/m}^2\text{K}$  is assumed for the convection of the lubricant flow [23]. The convection at the gears is neglected, since it is already included in the energy balance of the gears. The convection at the rotating shaft is calculated according to GROßMANN/JUNGNICKEL [18]. The shafts are represented by rotating smooth cylinders for heat transfer at the inner walls of the housing. According to RECKNAGEL, the heat transfer coefficient from the individual components, like gears, shafts or nuts is calculated with **Formula 3** [29]. The results are shown in Figure 11 on the left side.

$$\frac{1}{\alpha_{\text{shaft, housing}}} = \frac{1}{\alpha_{\text{shaft, air}}} + \frac{1}{\alpha_{\text{air, housing}}} \quad (3)$$

The heat transfer coefficient from the gears and chamber separations to the housing is  $\alpha_{\text{gears} \rightarrow \text{housing}} = 150\text{ W/m}^2\text{K}$ , between contact surfaces and housing its  $\alpha_{\text{contact surface} \rightarrow \text{housing}} = 75\text{ W/m}^2\text{K}$  and between the nut and the housing its  $\alpha_{\text{nut} \rightarrow \text{housing}} = 68\text{ W/m}^2\text{K}$ .

### Convection

$\alpha_{\text{TG, warm}}$ :	19.5 W/m <sup>2</sup> K
$\alpha_{\text{TG, cold}}$ :	15.09 W/m <sup>2</sup> K
$\alpha_{\text{TG, Clamping field}}$ :	6.3 W/m <sup>2</sup> K
$\alpha_{\text{TG, Oil}}$ :	300 W/m <sup>2</sup> K
$\alpha_{\text{gears} \rightarrow \text{housing}}$ :	150 W/m <sup>2</sup> K
$\alpha_{\text{contact surface} \rightarrow \text{housing}}$ :	75 W/m <sup>2</sup> K
$\alpha_{\text{nut} \rightarrow \text{housing}}$ :	68 W/m <sup>2</sup> K

### Radiation

$\varepsilon_{\text{housing}}$ :	0.6
$\varepsilon_{\text{clamping field}}$ :	0.94
$\varepsilon_{\text{shaft}}$ :	0.49

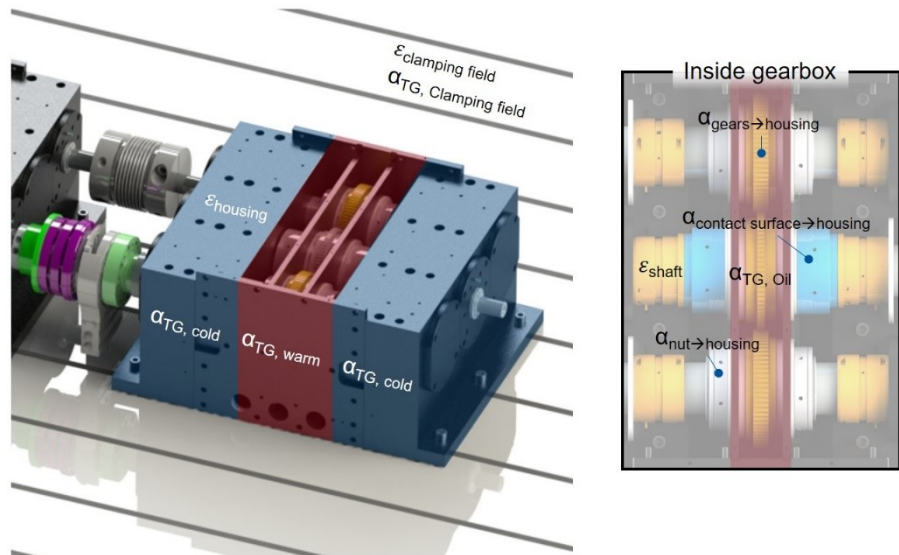


Figure 11 – Overview of the boundary conditions of the test gearbox

## Contactless seals

At the walls of the sealing, convection is assumed to be due to the oil volume flow with  $\alpha_{\text{oil, TG}} = 300\text{ W/m}^2\text{K}$  based on the same assumptions as in the "warm section". At the inner part of the sealing, convection is assumed to occur at the rotating cylinder, since here the shaft is presumably not completely or only slightly wetted by oil, and partial oil splashes back from the walls of the sealing. The cooling by inflowing air is neglected in the model. In the remaining areas, convection between shafts and air and convection in the narrow gap are assumed according to JUNGNICKEL 2010 [18].

## Journal bearings

The heat transfer of the journal bearings into the housing is calculated according to **formula 4**.

$$\alpha_{\text{bearing}} = \alpha_{\text{housing}} \cdot \frac{A_{\text{housing}}}{A_{\text{bearing}}} = 1240.41\text{ W/m}^2\text{K} \quad (4)$$

$\alpha_{\text{bearing}}$	Heat transfer coefficient bearings	[W/m <sup>2</sup> K]	$A_{\text{bearing}}$	Bearing surface	[m <sup>2</sup> ]
$\alpha_{\text{housing}}$	Heat transfer coefficient housing	[W/m <sup>2</sup> K]	$A_{\text{housing}}$	Housing surface	[m <sup>2</sup> ]

## 5.2 Simulated temperature distribution on the test gearbox

Under the assumptions and boundary conditions listed, the temperature distribution, heat flows and thermal expansion of the test gearbox were simulated with ANSYS. Figure 12 shows the results of the thermal simulation. The test gearbox heats up to a maximum temperature of  $T_{\text{max}} = 178.59^{\circ}\text{C}$ . The power loss, which is dissipated from the test gearbox to the environment accounts to  $P = 4.2 \text{ kW}$ . The main part of the heat is dissipated via the oil flow (see **chapter 3.3**) which is defined as an input variable in the simulation. Via the tooth mesh in the test gearbox  $P = 80 \text{ kW}$  are dissipated. The total loss of the bearings in the test gearbox is  $P \sim 28 \text{ kW}$ . The heat output, which is emitted to the environment, is divided as follows.

The clamping field emits  $Q_{\text{conv, clamping}} = 1.18 \text{ kW}$  via convection and  $Q_{\text{rad, clamping}} = 0.706 \text{ kW}$  via radiation to the ambient air. Via the warm part of housing  $Q_{\text{conv, housing, warm}} = 0.800 \text{ kW}$  is transferred convectively and  $Q_{\text{conv, housing, cold}} = 0.962 \text{ kW}$  via the cold housing part to the surrounding air. Additionally  $Q_{\text{rad, housing}} = 0.617 \text{ kW}$  is transferred from the housing to surrounding air by radiation.

The temperature at the sealing gaps results in negligible radial thermal expansion, so there is no solid-state contact and the sealing gap at maximum temperature still amounts  $s = 0.6 \text{ mm}$ . The axial expansion of the gearbox shafts can also be classified as not critical according to the simulation, so that safe operation under full thermal load is guaranteed. The pinion shaft expands by  $\Delta l_{\text{pinion shaft}} = 0.53 \text{ mm}$  and the wheel shafts by  $\Delta l_{\text{wheel shaft}} = 0.43 \text{ mm}$ . This expansion has to be considered in the design of the axial moveable sealings to prevent solid state contact on the one hand and to ensure sufficient sealing of the gearbox housing on the other hand.

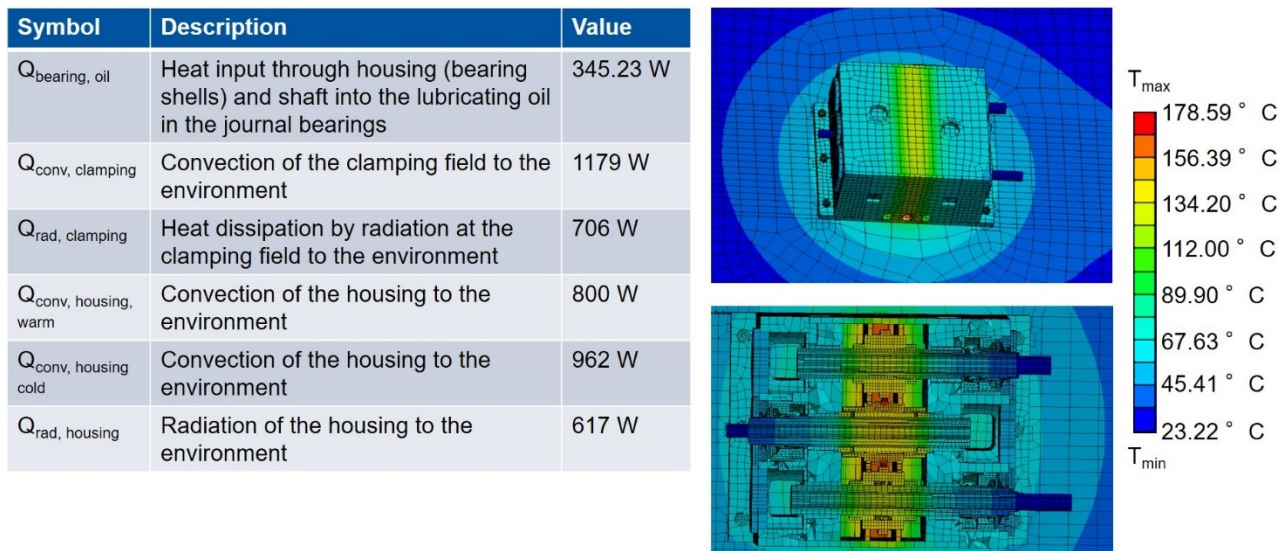


Figure 12 – Results thermal simulation of the test gearbox with ANSYS

### 1. Summary and Conclusion

Aircraft engines can be made more efficient by integrating planetary gears. In such an application, the planetary gears experience very high load cycles under fully reversed bending loads. Pulsator test rigs, which nowadays offer the possibility to perform UHCF investigations, can only be used for purely pulsating loading of gears. Therefore, for the investigation of the UHCF tooth root load carrying capacity under fully reversed bending load, a back-to-back test rig is required. Back-to-back test rigs usually have speeds of  $n = 3000 \text{ rpm}$ , which makes investigations in the UHCF range take a very long time. Therefore, a high-speed back-to-back test rig was developed.

---

One aim of the report is to define the operating parameters of this high-speed back-to-back test rig. Additionally the thermal behavior and thermal expansion of the components is checked by a thermal simulation with ANSYS. The test rig design is transferred to the SIMPACK multi-body simulation and the dynamic operating behavior is analyzed. Additionally, the dynamic loads from SIMPACK are compared to the values of the  $K_V$  factor according to method B of ISO 6336 and the operating parameters of the high-speed back-to-back test rig are defined.

The test rig uses a shifting helical gear for load application, which realizes torque control during operation as well as a compact design. The analysis of the dynamic torque in the test and reference gearbox during run-up shows that the dynamic loads occurring in the test gearbox are greater compared to the reference gearbox. The local torque maxima are caused by the excitation of the torsional natural frequencies of the shafts by the tooth mesh frequency and its harmonics. The dynamic load in the test and reference gearbox from SIMPACK is compared with the dynamic factor according to method B of ISO 6336. The dynamic factor according to ISO 6336 underestimates the dynamic loads of the test gearbox at the operating speed  $n_1 = 12000$  rpm whereas the additional loads in the reference gearbox are overestimated. Furthermore, the vibration behavior is decisively determined by the torsional natural frequencies of the gearbox shafts, which are not taken into account in the standard calculation according to method B. Since resonances do not occur above  $n_1 = 4000$  rpm, the operating point does not have to be restricted. Below  $n_1 = 4000$  rpm and above the minimum speed of the journal bearings, it makes sense to load the gearing with half the test torque in order to avoid preliminary damage due to tooth flank lift off. According to the differences between standard calculation approach and multi-body simulation it is particularly useful for high-speed applications to use multi-body simulations considering all degrees of freedom. Furthermore, the resonances at low rotational speeds require a gradual ramp up of torque and speed during the run-up of the test rig. Using this approach preliminary damages of the test gears e.g. caused by flank lift off can be prevented.

The thermal simulation of the test rig estimates the power loss of the test rig to the surrounding room and is used to check the functionality of the test rig under thermal expansion at maximum operating temperature. In addition to the heat dissipated by the cooling oil volume flow ( $P = 390$  kW), a heat loss of  $P = 4.2$  kW was obtained, which is dissipated by the test gearbox to the ambient air. For a safe and continuous operation it has to be ensured that the room ventilation is powerful enough to remove the losses. The simulation also showed that the functionality of the test rig is fully given at maximum temperature and thermal expansion. The maximal thermal expansion of the shafts in axial length is  $\Delta l_{\text{pinion shaft}} = 0.53$  mm and  $\Delta l_{\text{wheel shaft}} = 0.43$  mm. The sealing gaps expand in radial direction but at the maximum temperature there is still a gap of  $s = 0.6$  mm. The amount of thermal expansion makes clear that a simulation of the thermal expansion for high testing temperatures as well as for high rotational speeds is necessary. Thereby the fits of bearings and seals can be chosen as close as possible to ensure a safe operation.



---

## Bibliography

1. Aerosieger.de (2016) A340-Triebwerk überschreitet 100.000 Flugstunden. <https://www.aerosieger.de/news/8623/a340-triebwerk-ueberschreitet-100000-flugstunden.html/>. Zugegriffen: 25. März 2020
2. Barrot A, Paredes M, Sartor M (2016) Determining both radial pressure distribution and torsional stiffness of involute spline couplings. *J. Mech. Eng. Sci.* 220(12):1727–1738. doi:10.1243/0954406JMES285
3. Baud S, Vex P (2002) Static and Dynamic Tooth Loading in Spur and Helical Geared Systems-Experiments and Model Validation. *J. Mech. Des.* 124(2):334–346. doi:10.1115/1.1462044
4. Bosch M (1965) Über das dynamische Verhalten von Stirnradgetrieben unter besonderer Berücksichtigung der Verzahnungsgenauigkeit. Diss., RWTH Aachen University
5. Carl CF (2014) Gehörbezogene Analyse und Synthese der vibroakustischen Geräuschanregung von Verzahnungen. Diss., RWTH Aachen University
6. Ciulli E (2019) Experimental rigs for testing components of advanced industrial applications. *Friction* 7(1):59–73. doi:10.1007/s40544-017-0197-z
7. Donath B (1983) Berechnung der inneren dynamischen Zahnkräfte ein- und zweiflankiger Zylinderradgetriebe mit Schrägverzahnung. Diss., TU Dresden
8. Duchstein P (2013) Getriebeturbofan und konventioneller Turbofan: Ein Vergleich auf der Basis stationärer Leistungsrechnungen, 1. Aufl. Diplomica Verlag GmbH, s.l.
9. Eberhard P, Ziegler P (Hrsg) (2011) Rädertriebssimulation II. Berechnung von dynamischen Spannungen und Kontaktkräften in Zahnradstufen bei stoßartigen Belastungen unter Verwendung elastischer Ansätze, Frankfurt a.M.
10. Früh P (2008) Dynamik von Zahnradgetrieben. Modellbildung, Simulation und experimentelle Analyse. Diss., Universität Rostock
11. Gacka A (2013) Entwicklung einer Methode zur Abbildung der dynamischen Zahneingriffsverhältnisse von Stirn- und Kegelsatzradpaaren. Diss., RWTH Aachen University
12. Geiser H (2002) Grundlagen zur Beurteilung des Schwingungsverhaltens von Stirnrädern. Diss., TU München
13. Gerber H (1984) Innere dynamische Zusatzkräfte bei Stirnradgetrieben. Modellbildung, Innere Anregung und Dämpfung. Diss., TU München
14. Gold PW (1979) Statisches und dynamisches Verhalten mehrstufiger Zahnradgetriebe. Diss., RWTH Aachen University
15. Graham-Rowe D (2010) More Efficient Jet Engine Gets in Gear. Airbus will adopt a type of jet engine intended to improve fuel efficiency. <https://www.technologyreview.com/s/421992/more-efficient-jet-engine-gets-in-gear/>. Zugegriffen: 25. März 2020
16. Heider MK (2012) Schwingungsverhalten von Zahnradgetrieben. Beurteilung und Optimierung des Schwingungsverhaltens von Stirnrad und Planetengetrieben. Diss., TU München
17. Joop M (2018) Die Fresstragfähigkeit von Stirnrädern bei hohen Umfangsgeschwindigkeiten bis 100 m/s, Ruhr-Universität Bochum
18. Jungnickel G (2010) Simulation des thermischen Verhaltens von Werkzeugmaschinen: Modellierung und Parametrierung

- 
19. Linke H (1969) Untersuchungen zur Ermittlung dynamischer Zahnkräfte von einstufigen Stirnradgetrieben mit Geradverzahnung. Diss., TU Dresden
  20. Möllers W (1982) Parametererregte Schwingungen in einstufigen Zylinderradgetrieben. Einfluß von Verzahnungsabweichungen und Verzahnungssteifigkeitsspektren. Diss., RWTH Aachen University
  21. MTU (2020) Pratt & Whitney GTF Engines. <https://www.mtu.de/de/engines/zivile-triebwerke/narrow-body-and-regional-jets/gtf-triebwerksfamilie/>. Zugegriffen: 25. März 2020
  22. Müller R (1991) Schwingungs- und Geräuschanregung bei Stirnradgetrieben. Diss., TU München
  23. Niemann G, Winter H (2003) Maschinenelemente. Band 2: Getriebe allgemein, Zahnradgetriebe - Grundlagen, Stirnradgetriebe, 2. Aufl, Bd 2. Springer, Berlin
  24. Norm (1987) Tragfähigkeitsberechnung von Stirnrädern. Einführung und allgemeine Einflußfaktoren (3990 Teil 1). Beuth, Berlin
  25. Norm (2004) Fundamental rating factors and calculation methods for involute spur and helical gear teeth (2101-D04). American Gear Manufacturers Association, Virginia
  26. Norm (2006) Zahnräder. FZG-Prüfverfahren. FZG-Prüfverfahren A/8,3/90 zur Bestimmung der relativen Fresstragfähigkeit von Schmierölen (14635 Teil 1). Beuth, Berlin
  27. Norm (2006) Calculation of load capacity of spur and helical gears. Basic principles, introduction and general influence factors (6336 Teil 1). ISO copyright office, Geneva
  28. Plohr M, Lecht M, Otten T, Döpelheuer A, Hemmer H (2006) AERO-ENGINE TECHNOLOGY TO COPE WITH ACARE GOALS ICAS 2006 proceedings. Hamburg, Germany, 3 - 8 September, 2006
  29. Recknagel (2017) Taschenbuch für Heizung + Klimatechnik 78. Ausgabe 2017/2018: einschließlich Trinkwasser- und Kältetechnik sowie Energiekonzepte. DIV Deutscher Industrieverlag GmbH, München
  30. SIMPACK GmbH (2017) SIMPACK Documentation - Release 2018. Firmenschr., SIMPACK GmbH
  31. Trippe M, Lövenich J, Malinowski O, Brecher C, Brimmers J, Neus S (2021) Untersuchungskonzept zum Einfluss hoher Dehnraten auf die Zahnfußtragfähigkeit. Forsch. Ingenieurwes. doi:10.1007/s10010-021-00440-7
  32. Walton JF, JR., Ku C-PR, Lund JW (1994) An investigation of angular stiffness and damping coefficients of an axial spline coupling in high-speed rotating machinery
  33. Weber C, Banaschek K (1955) Formänderung und Profilrücknahme bei gerad- und schrägverzahnten Rädern, 2. Aufl. Vieweg, Braunschweig
  34. Weck M, Winter H, Winkler A, Rettig H (Hrsg) (1975) Innere dynamische Zusatzkräfte an Zahngetrieben, Frankfurt a.M.
  35. Winkler A (1975) Über das dynamische Verhalten schnellaufender Zylinderradgetriebe. Diss., RWTH Aachen University